

The sequence of low and high mass star formation in the young stellar cluster IRAS 19343+2026

D. K. Ojha^{1*}, M. S. N. Kumar², C. J. Davis³ and J. M. C. Grave²

¹ *Tata Institute of Fundamental Research, Homi Bhabha Road, Mumbai-400005, India*

² *Centro de Astrofísica da Universidade do Porto, Rua das Estrelas, 4150-762 s/n Porto, Portugal*

³ *Joint Astronomy Center, 660 N. A'ohōkū Place, University Park, Hilo, HI 96720, USA*

ABSTRACT

BVRIJHK photometry, *Spitzer*-GLIMPSE photometry and *HK* band spectroscopy were used to study the stellar content of IRAS 19343+2026, a (proto)star/cluster candidate, located close to the Galactic plane. The data suggest that IRAS 19343+2026 is a rich cluster associated with a massive protostar of $7.6 M_{\odot}$ with an age of $\sim 10^5$ yr. Three point sources in the vicinity of the far-infrared (FIR) peak are also found to be early B type stars. The remaining (predominantly low mass) members of the cluster are best represented by a 1 - 3 Myr pre-main-sequence (PMS) population. *HK* band spectra of two bright and five faint point sources in the cluster confirm that the results obtained from the photometry are good representations of their young stellar object (YSO) nature. Thus, IRAS 19343+2026 is a young cluster with at least four early B-type stars classified as young (10^4 - 10^5 yr), that are surrounded by a somewhat older (1 - 3 Myr) population of low mass YSOs. Together, these results argue for a scenario in which low mass stars form prior to massive stars in a cluster forming environment. We compute the Initial Mass Function (IMF) for this cluster using the *K*-band luminosity function; the slope of the IMF is shallower than predicted by the Salpeter's mass function. The cluster mass, M_{total} , is estimated to be in the range $\sim 307 M_{\odot}$ (from the data completeness limit) - $585 M_{\odot}$ (extrapolated down to the brown dwarf limit, assuming a certain IMF).

Key words: stars:formation – ISM: HII regions – infrared: stars

1 INTRODUCTION

One of the important issues in understanding massive star formation is the sequence of formation of low and high mass stars in a cluster forming environment (Zinnecker & Beuther 2008). This issue has relevance when explaining the nature of massive star formation in terms of either: (a) low to intermediate mass stars accumulating matter while evolving toward the main sequence, or (b) competitive accretion of massive cores in a star forming cloud (McKee & Tan 2002; McKee & Tan 2003; Zinnecker & Yorke 2007). Observations of embedded clusters generally display mass segregated configurations, with a few young high mass stars located at the cluster centers (McNamara & Sekiguchi 1986, and references therein). Although an age estimation for the lower mass pre-main-sequence (PMS) population is possible using evolutionary tracks and colour-magnitude (CM) diagrams, the same is not true for massive stars, since they are usually only a few in number. Therefore, it is necessary to investigate clusters around high mass protostellar object candidates, where the youth of the massive stars is made clear by various other signposts, such as outflows, compact HII regions, excess FIR emission, and so on. Kumar, Keto & Clerkin (2006) searched for clustering around a sample of high mass protostellar objects and found 54 embedded clusters among 215 candidates. The detection of clustering in about 25% of the sources (all targets located away from the Galactic mid-plane) suggests that at least one generation of low mass stars has already formed around these massive protostellar candidates. However, the Two Micron All Sky Survey (2MASS) data used by these authors did not effectively uncover the lower mass population; the 2MASS data were not deep enough to characterise the remaining cluster members. In contrast, a follow-up of the same data sets by Kumar & Grave (2007) using the *Spitzer*-GLIMPSE survey (Churchwell et al. 2009) did not find any clustering for the sources in the Galactic mid-plane. This mid-infrared survey should have been more successful at finding clusters because of the better dust penetration.

In this paper, using high quality optical and infrared observations of a high mass protostellar object in the Galactic mid-plane, we attempt to examine such discrepancies, measure the stellar content, and understand the sequence of low and high mass star formation in the associated cluster. The high quality NIR photometric and spectroscopic data are combined with *Spitzer* IRAC and MIPS observations to study the target. Study of the massive star content is particularly aided by radiative transfer modelling of the SED. The target,

IRAS 19343+2026, is a high mass protostellar object candidate located at a kinematic distance (measured using NH_3 line velocities) of 4.2 kpc, with a FIR luminosity of $2.7 \times 10^4 L_\odot$ (Molinari et al. 1996). This cluster is detected in the GLIMPSE survey (cluster 24 of Mercer et al. 2005). Section 2 describes the detailed observations. The photometric, spectroscopic and SED modelling results are also presented in this section. The implications of the results are discussed in Section 3. We then summarize our conclusions in Section 4.

2 OBSERVATIONS AND DATA REDUCTIONS

2.1 J, H, K imaging and photometry

NIR photometric imaging observations were made at the 3.8 m United Kingdom Infrared Telescope (UKIRT) with the facility imager UFTI (Roche et al. 2002). UFTI houses a HAWAII-1 1024×1024 pixel array. The UFTI plate scale of $0.091''$ gives an available field of view (FOV) of $\sim 90''$. Photometric observations through J ($\lambda = 1.25 \mu\text{m}$, $\Delta\lambda = 0.16 \mu\text{m}$), H ($\lambda = 1.64 \mu\text{m}$, $\Delta\lambda = 0.29 \mu\text{m}$) and K ($\lambda = 2.20 \mu\text{m}$, $\Delta\lambda = 0.34 \mu\text{m}$) broad-band filters were obtained for the IRAS source during the night of 26th June 2002. An integration time of 60 sec was used in each of the J , H and K band filters; averaging jittered exposures yielded a total exposure time of 540 seconds in each band. The mean seeing measured was $0.6''$ in the K -band images. A nine point (3×3) jittered observing sequence was executed to obtain data that provided final mosaics with a total FOV of $\sim 115'' \times 115''$. We note that the signal-to-noise ratio at the edges of these mosaics is lower than within the central $90''$ area. Standard data reduction techniques involving dark subtraction and median-sky-flat-fielding of the jittered object frames were applied. The K -band image of IRAS 19343+2026 is shown in Fig. 1, with an overlay of *Spitzer* MIPS $24 \mu\text{m}$ contours.

Subsequent to our observations, this region was recently covered by the UKIRT Infrared Deep Sky Survey (UKIDSS; Lawrence et al. 2007) Galactic Plane Survey (GPS). The GPS is an ambitious survey of the Northern Galactic plane (Lucas et al. 2008). The aim of the survey is to map 1800 square degrees of the plane ($|b| < 5 \text{ deg}$) in J , H , and K to a depth of $J \sim 20.0$, $H \sim 19.1$, $K \sim 19.0$ at sub-arcsecond resolution. UKIDSS employs the Wide Field Camera (WFCAM; Casali et al. 2007) at UKIRT. WFCAM contains four Rockwell Hawaii-II (HgCdTe 2048×2048 pixel) arrays spaced by 94% in the focal plane. With a pixel scale of $0.4''$ the field of view of each array is $13.7'$. All UKIDSS survey data are reduced by the Cambridge Astronomical Survey Unit (CASU) and are distributed via the WFCAM

Science Archive (WSA¹). The GPS data sensitivity is comparable to our observations ($K = 18$ mag), albeit with a relatively poor seeing ($1''$) and a coarse pixel scale of $0.2''$. Fig. 2 shows the 50th nearest-neighbour (NN) density map (Schmeja, Kumar & Ferreira 2008, and references therein) of the UKIDSS K -band source counts. From this figure the cluster center was found to be at $\alpha_{2000} = 19^{\text{h}}36^{\text{m}}31^{\text{s}}$, $\delta_{2000} = +20^{\circ}33'03''$. For the purpose of evaluating the foreground/background contamination, we have chosen a “control region” $\sim 2'$ North of the cluster center at $\alpha_{2000} = 19^{\text{h}}36^{\text{m}}32^{\text{s}}$, $\delta_{2000} = +20^{\circ}34'48''$ (see Fig. 2).

We utilised tasks available in the Image Reduction and Analysis Facility (IRAF) package for our photometric analysis. DAOFIND was used to identify sources in each image. A point spread function (PSF) model was computed by choosing stars of different brightness that were well spaced out in our images. Photometry was performed using the DAOPHOT package. Aperture corrections were determined by performing multi-aperture photometry on the PSF stars. The instrumental magnitudes were calibrated to the absolute scale using observations of UKIRT faint standard stars; FS 29, FS 35 & FS 140 (Hawarden et al. 2001). These standards were observed over a range in airmass (1.05 - 1.79) that was comparable to the target observations. The resulting photometric data are in the natural system of the Mauna Kea Consortium Filters (Simons & Tokunaga 2002). For the purpose of plotting these data, we converted magnitudes to the Bessell & Brett (1988) (hereafter BB) system, since the main-sequence references are in the BB system. To do this, we first converted the Mauna Kea system to the CIT system and then to the BB system using equations given by Hawarden et al. (2001).

Representative sub-images consisting of stars and nebulosity were chosen to determine the completeness limits. Limits were established by manually adding and then detecting artificial stars of differing magnitudes. By determining the fraction of stars recovered in each magnitude bin, we have deduced 90% completeness limits of 19.3, 19.0 and 17.5 magnitudes in the J , H and K bands, respectively. Our observations are absolutely complete (100%) to the levels of 17.3, 17.2 and 16.2 magnitudes in J , H and K , respectively. Photometric analysis was carried out using data with photometric errors of less than 0.1 mag. Absolute position calibration was achieved using the coordinates of a number of stars from the 2MASS catalog. The astrometric accuracy of the data presented in this work is better than $0.5''$.

¹ <http://surveys.roe.ac.uk/wsa/index.html>

The sources are saturated at $K < 12$. For such bright sources, 2MASS Point Source Catalog data were used.

We also extracted source magnitudes from the UKIDSS images using the methods described above, although our UFTI images (rather than 2MASS data) were used to calibrate the UKIDSS data. The UKIDSS observations were used to create a density map of the region (see Figure 2), and to obtain photometry over a larger area than was observed with UFTI.

2.2 HK band spectroscopy

NIR HK band spectra of several stars in the target field were obtained using the UKIRT 1 - 5 μm Imager Spectrometer (UIST) (Ramsay Howat et al. 2004) on the night of 21st July 2005. UIST has a 1024×1024 InSb array and a 0.12 arcsec per pixel plate scale. The observations were made using a 120 arcsec long slit with a width of 4 pixels. The HK grism was used, which allowed complete wavelength coverage from 1.395 μm to 2.506 μm with a spectral resolution of $R \simeq 500$. The exposure time per frame was set to 60 sec; 8 exposures were obtained per slit position, resulting in a total integration time of 8 minutes. The 120" long slit was aligned carefully to cover multiple sources in a single position. This configuration and integration time provided a 5σ point source sensitivity of ~ 16 mag in the HK bands. The target was nodded up and down the slit in an ABBA fashion; B exposures were subtracted from adjacent A exposures to give sky-subtracted 2-dimensional spectral images. The spectral images were averaged and the positive and negative beams of stellar spectra were then optimally extracted. These resulting "group" spectra were corrected for telluric absorption and flux calibrated by division with a similarly-observed standard star spectrum. The G2V source HIP102189 was used for this purpose. (Note that the standard star spectrum was first divided by a black body template of appropriate temperature to preserve the intrinsic slopes of the calibrated target spectra.)

The initial reduction steps (i.e. dark and flat correction) were performed using the UKIRT/Starlink data reduction pipeline ORAC-DR (Cavanagh et al. 2003); the extraction and analysis of the spectra were done with IRAF and IDL.

2.3 Optical Imaging and Photometry

Bessell $BVRI$ images of the region associated with the IRAS 19343+2026 region were obtained with the 2-m Himalayan *Chandra* Telescope (HCT) of the Indian Astronomical Ob-

servatory (IAO), Hanle, India, on 16th March 2005. The Hanle Faint Object Spectrograph Camera (HFOSC), which is equipped with a SITe $2K \times 4K$ pixel² CCD, was used. With a pixel scale of $0.296''$, the FOV of HFOSC, where only the central $2K \times 2K$ region is used for imaging, is $\sim 10 \times 10$ arcmin². Further details on the telescope and the instrument can be found at <http://www.iap.res.in/iao/hfosc.html>. Observations were carried out under good photometric sky conditions. The typical seeing [full width at half-maximum (FWHM)] during the period of observations was $\sim 1.8''$. Bias and flat frames were obtained at the beginning and at the end of the observing night. Photometric standard stars around the SA 111-775 region (Landolt 1992) were observed to obtain the transformation coefficients.

The data reduction was again carried out using IRAF tasks. Object frames were flat-fielded using median-combined normalized flat frames. Identification and photometry of point sources were performed using the DAOFIND and DAOPHOT tasks, respectively. Photometry was obtained using the PSF algorithm ALLSTAR in the DAOPHOT package (Stetson 1987). The residuals to the photometric solution were ≤ 0.05 mag.

2.4 Spectral energy distribution modelling

The *Spitzer*-GLIMPSE survey IRAC and MIPS images and IRAC photometry of this target were analysed using the IRSA-IPAC image cutouts and GATOR facilities. MIPS $24 \mu\text{m}$ photometry was extracted using the APEX single frame pipeline on the Post-Basic-Calibrated Data. The photometric data in the *Spitzer* bands ($3.6 - 24.0 \mu\text{m}$) were combined with 2MASS NIR photometry and IRAS data to construct SEDs for the four brightest sources in the region – the massive young star candidates. The online SED fitting tool developed by Robitaille et al. (2007) was used to fit the resulting SEDs in the $1 - 24 \mu\text{m}$ bands. The SED fitting tool is based on matching the observed SEDs with a large grid of precomputed radiative transfer models. The models assume an accretion scenario with a star, disk, envelope and bipolar cavity, all under radiative equilibrium. While the mass and age of the star are uniformly sampled within the grid limits, the radius and temperature are interpolated using evolutionary models. The optical and NIR data points constrain the stellar parameters, the mid-infrared fluxes constrain the disk parameters and the far-infrared points are sensitive to envelope emission (see Robitaille et al. 2006 for more details). The SED fitting tool has been successfully tested on low mass stars and shown to produce reliable estimates of physical parameters by comparing against values obtained by other independent

measurements. Grave & Kumar (2009) discuss the implementation of this tool on a large sample of massive protostellar objects. For fitting purposes a 10% error was assumed on all fluxes. The weighted mean (weights being the inverse of χ^2) of each physical parameter was computed for all models that satisfied the criteria $\chi^2 - \chi^2_{best} < 3$, where χ^2 is the statistical goodness of fit parameter measured per data point.

3 RESULTS

A rich cluster of stars can be seen in our *K*-band image (see Fig. 1), the brightest stars in the center of the field coinciding with the peak of the MIPS 24 μm contours. The two straight lines in Fig. 1 mark the slit positions used to obtain the spectra of the stars numbered 1 to 7. Stars 1, 3 and 8 were modelled using 1 - 24 μm SEDs. Star 9 was not detected in the MIPS 24 μm band. The brightest stars in the field are expected to be massive stars, while the fainter population represents the low mass members. In Fig. 3 (see the online electronic version of this article for a colour plot) a colour composite of the *Spitzer* infrared images is shown. The three-colour composite image was made using the *Spitzer* IRAC 3.6 μm , IRAC 8.0 μm and MIPS 24 μm images coded as blue, green and red, respectively. Notice the bipolar shape of the nebula and the FIR excess emission appearing as red. The stars 8 & 9 are associated with excess emission at 24 μm , as can be seen from the red colour surrounding these two stars. Also, the rich cluster of stars seen in Fig. 1 is not visible in this composite image. We will comment further on this issue in Sect. 4. In the following, we first discuss the photometric analysis of the whole sample, then the IMF of the cluster region, followed by spectra of the seven representative sources (stars 1-7), and finally the SED fitting analysis of the brighter massive star candidates.

3.1 Photometric Analysis

The *JHK* photometry of the point sources in the IRAS 19343+2026 region was used to construct colour-colour (CC) and CM diagrams. A combination of CC and CM diagrams made using various optical and infrared bands were then used to evaluate the membership of the cluster against a control field, and to evaluate the cluster properties. The total number of point sources (with magnitude errors < 0.1 mag), detected in the region shown in Fig. 1 was 333, 688 and 875 in the *J*, *H* and *K* bands, respectively. 307 stars are common to all three bands; 607 stars appear in the *H* and *K* bands. The UFTI *JHK* photometric data,

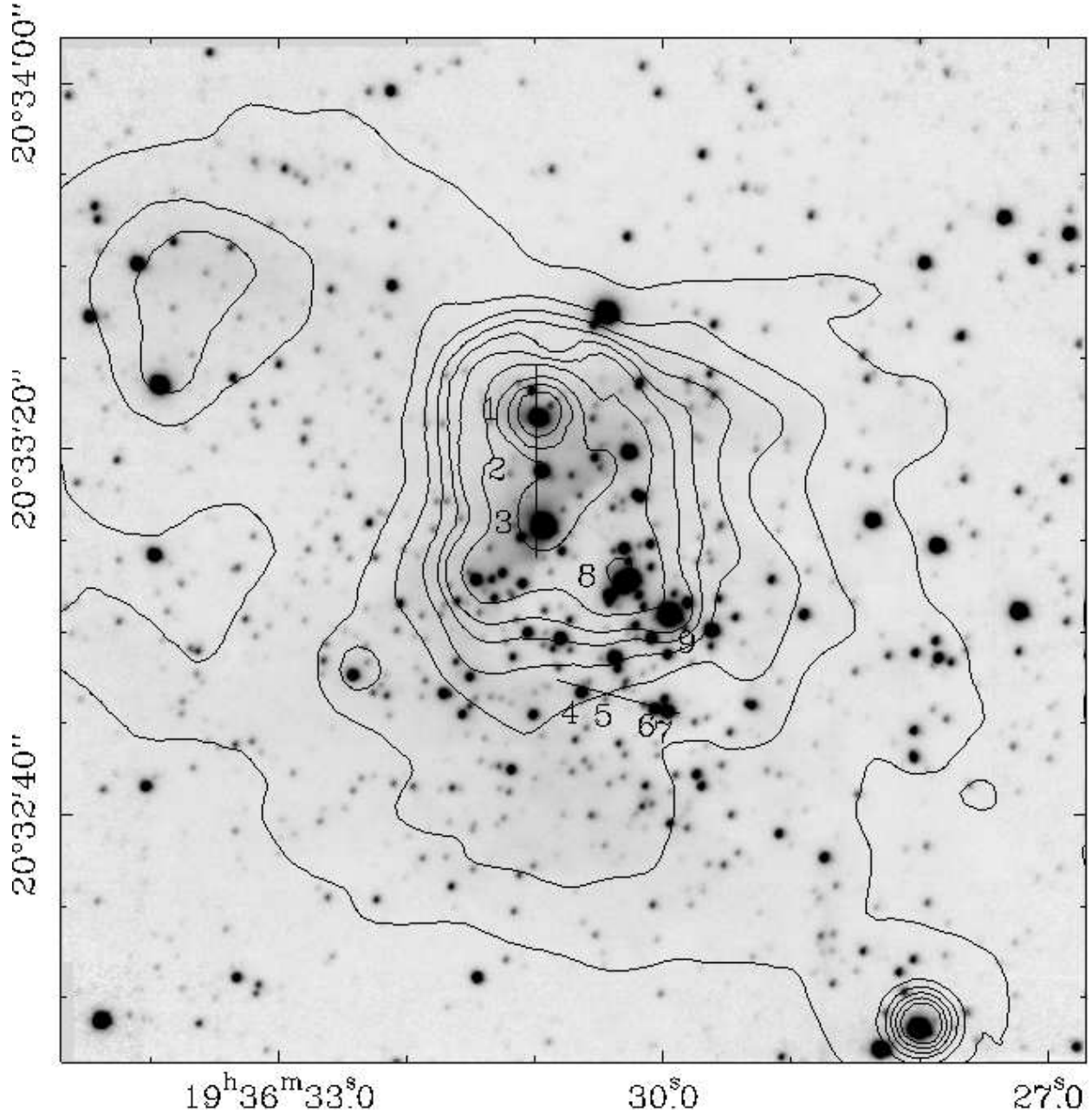


Figure 1. A K -band image of the IRAS 19343+2026 region shown with a logarithmic greyscale stretch. Contours represent the MIPS $24\ \mu\text{m}$ emission. The solid lines mark the positions of the slits used to obtain HK band spectra of the stars numbered 1–7; note that spectra were not obtained for the bright NIR sources labelled 8 and 9. The abscissa (RA) and the ordinate (DEC) are in J2000.0 epoch.

along with the positions of the stars, are given in Table A.1; the complete table is available in electronic form as part of the online material.

Photometry of the images obtained from the UKIDSS-GPS survey was performed over a larger area ($\sim 7' \times 7'$). The analysis of both the cluster and control regions was carried out in a similar way. In order to evaluate the mass function (see Sect. 3.2) of the cluster region, we have chosen a box size of $1.2'$ centered on the cluster and control regions, as mentioned earlier (see Sect. 2.1).

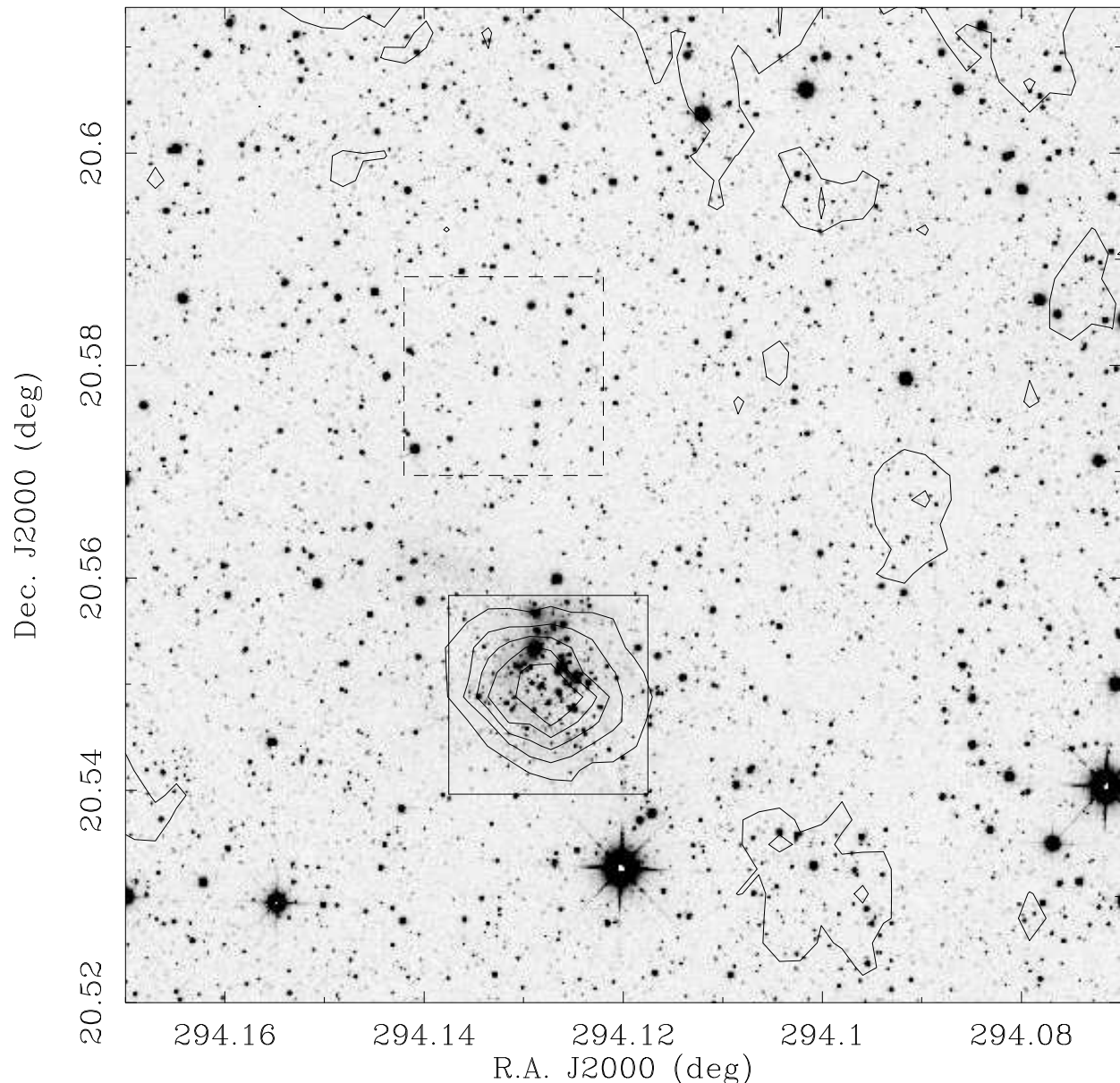


Figure 2. 50th nearest-neighbour density map of UKIDSS K -band source counts around the IRAS 19343+2026 region. The contours are plotted over the UKIDSS image; the contour level starts at 111 stars per arcmin² and increases in steps of 28 stars per arcmin². The solid and dashed boxes represent the chosen cluster and control field regions.

Fig. 4 shows the $J - H/H - K$ CC diagram for the cluster field. The solid (*bottom-left*) and broken heavy curves represent the main-sequence dwarf and giant stars, respectively. The dotted line indicates the locus of T Tauri stars (Meyer, Calvet & Hillenbrand 1997), while the dashed-dotted line represents the HAeBe locus (Lada & Adams 1992). The three dashed parallel lines are the reddening vectors. We adopt a slope consistent with $E(J - H)/E(H - K) = 1.9$ (BB system), which is appropriate to an interstellar reddening law of $R = 3.12$ (Whittet & van Breda 1980). The CC diagram was used to identify the reddened population that falls in the region occupied by T Tauri and HAeBe stars. Stars that lie

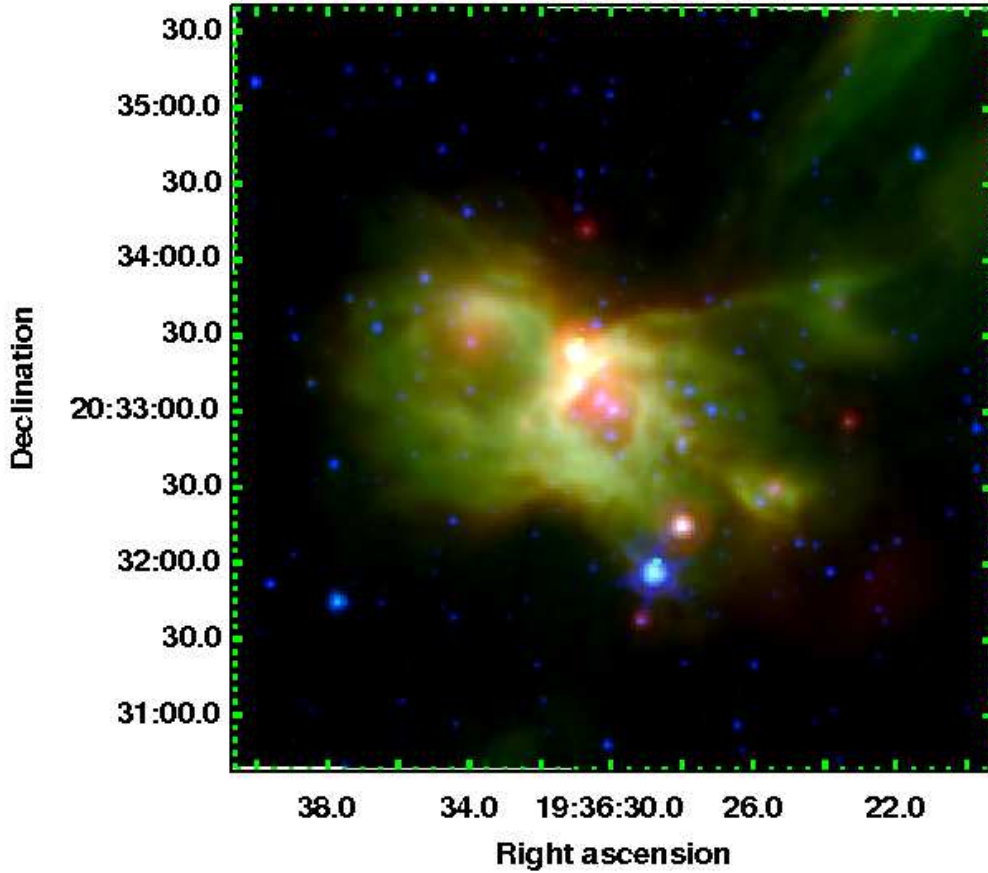


Figure 3. Three-colour composite made from *Spitzer* images (for a colour representation see the online electronic version of this paper). The MIPS 24 μm , IRAC Ch4 (8.0 μm) and IRAC Ch1 (3.6 μm) images are coded red, green and blue respectively. The abscissa and the ordinate are in J2000.0 epoch.

outside the region of reddened main-sequence objects (i.e. redward of the reddening line drawn from the base of the main-sequence dwarf branch, that is, redward of the middle of the three vectors) are YSOs with intrinsic colour excesses. We shall refer to these as “probable cluster members”. By de-reddening the stars on the CC diagram that fall within the first two reddening vectors (encompassing the main-sequence and giant stars) to the dwarf locus, a visual extinction (A_V) for each star was calculated. The individual extinction values range from 0 to 20 mag, resulting in an average extinction of $A_V = 7.6$ mag.

Fig. 5 shows the UKIDSS GPS $K/H - K$ CM diagram for the cluster and the control region. From the control region plot (*middle panel*) it is possible to clearly identify the dwarf and giant branches of the stellar population, i.e. sources with an $H - K$ colour of less than 1.0. In contrast, the cluster region (*left panel*) displays the dwarf branch (the group of stars running vertically at $H - K \sim 0.4$) and a significant number of stars with $H - K$ colours

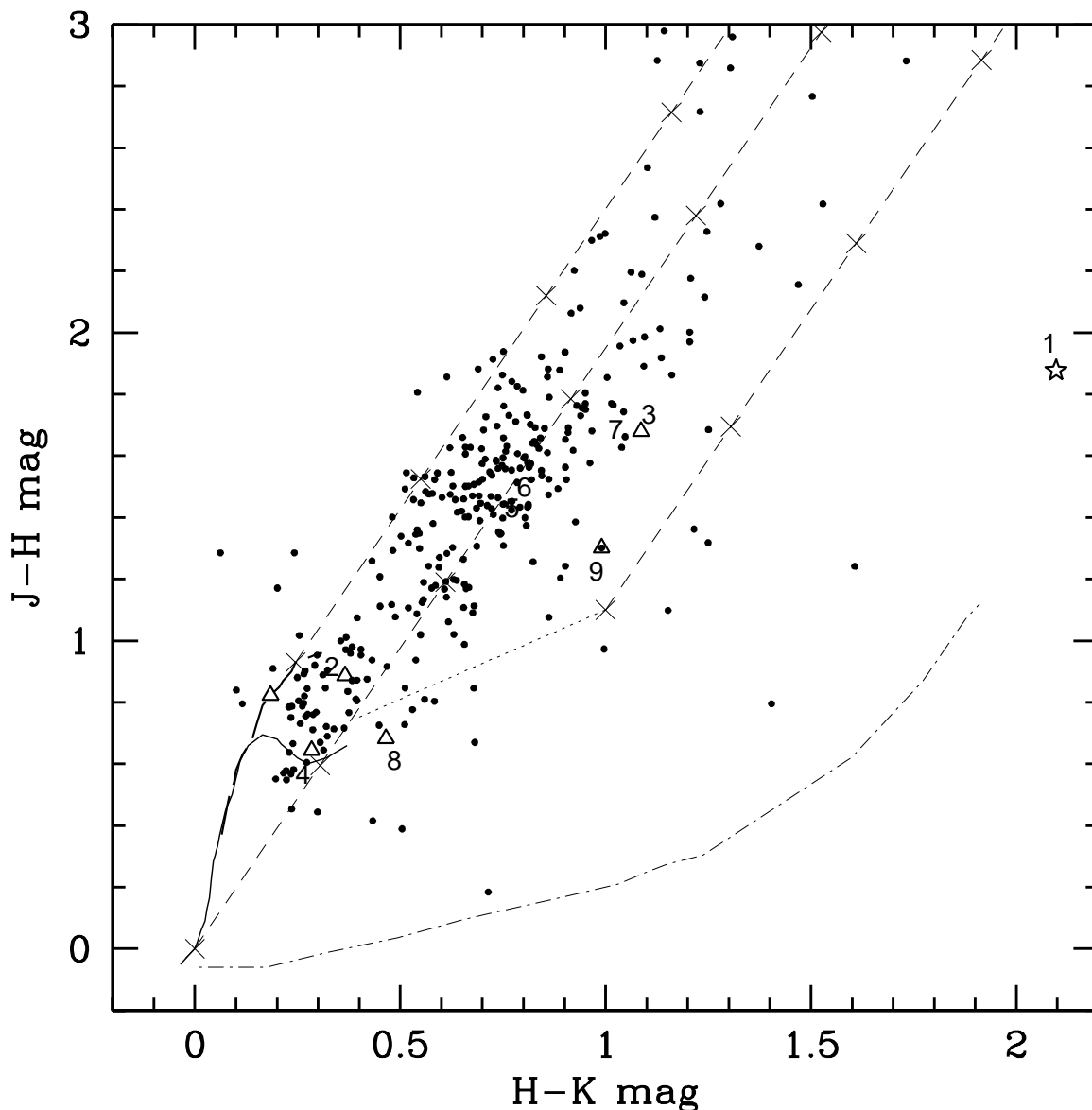


Figure 4. CC diagram of the region around IRAS 19343+2026 constructed from the UFTI data. The solid (*bottom-left*) and broken heavy curves represent the main-sequence dwarf and giant stars, respectively, taken from Bessell & Brett (1988). The dotted line indicates the locus of T Tauri stars (Meyer, Calvet & Hillenbrand 1997); the dashed-dotted curve represents the H A e Be locus (Lada & Adams 1992). The dashed parallel lines are reddening vectors on which crosses separated by $A_V = 5$ mag have been marked. The triangles mark the brightest NIR sources in the region, while the numbers refer to the sources labelled in Fig. 1. The star symbol (star 1) marks the $2 \mu\text{m}$ source that coincides with the FIR peak.

around 1. These stars are essentially cluster members which are also identified on the CC diagram as probable cluster members. The control field also has very few stars with $H - K < 1$ as compared to the cluster region. Therefore, we find that the contamination from foreground/background stars in our cluster region is minimal compared to the statistics of the probable cluster members. However, $H - K$ colour alone is no good for distinguishing between a reddened background star and a young star. Therefore, we have used a statistical

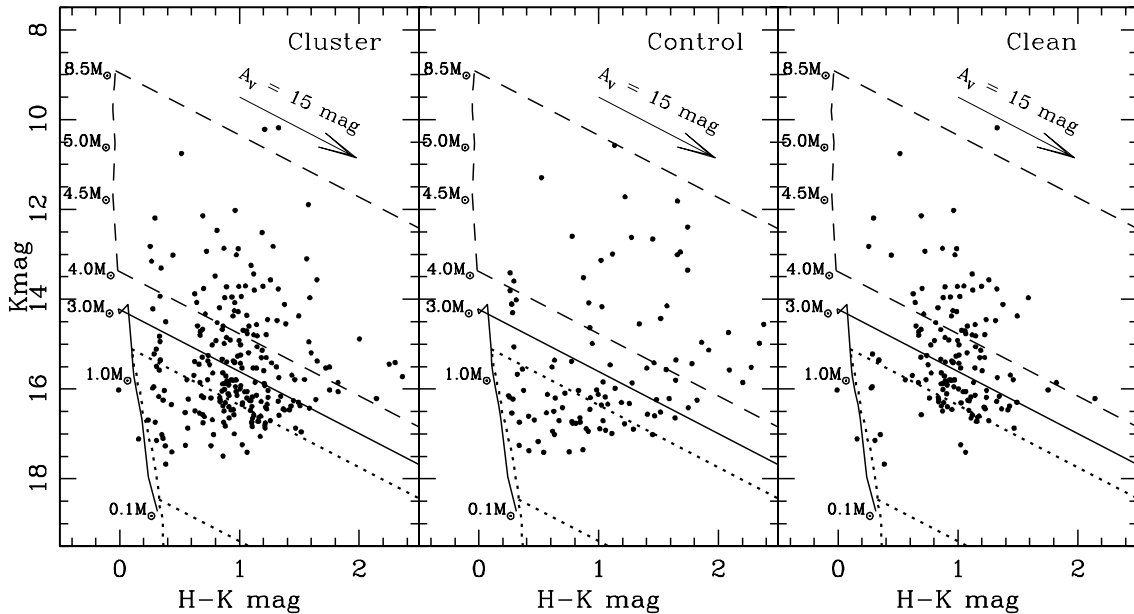


Figure 5. $K/H - K$ CM diagrams of the IRAS 19343+2026 cluster region (*left*), the control region (*middle*) and the statistically cleaned cluster region (*right*) from the UKIDSS GPS data. The solid and dotted curves show the PMS tracks from Palla & Stahler (1999) and Baraffe et al. (1998), respectively, for an assumed age of 3 Myr for low mass range ($M < 3 M_{\odot}$), while the dashed curve denotes the PMS track for 3 Myr age (Lejeune & Schaerer 2001) for intermediate mass range ($4 < M/M_{\odot} \leq 8.5$). The parallel slanting lines identify the reddening vectors.

approach to remove contaminating field stars from the $K/H - K$ CM diagram of the cluster region (we will discuss this further in detail in the following Sect. 3.2). The cluster member stars are clearly seen in the statistically cleaned CM diagram (*right panel*).

Our aim here is to estimate the approximate age of the lower mass population by comparing our data with theoretical evolutionary tracks. The low mass evolutionary tracks have been tested on various observational data of young stellar clusters and are thought to be good representations. The evolutionary models for high mass stars are more complicated and varied, however, and are not well tested against observational data sets. Therefore, we first use the pre-main-sequence (PMS) isochrone fitting for the lower mass population. Further, it should be noted that a CM diagram that uses only one colour may not be very effective in describing the less understood massive young stars.

Since the stellar photosphere's are better represented by shorter wavelength data such as the optical, J and H bands, we use these data when comparing source photometry with the model isochrones. In the region of Fig. 1, all optically detected stars in the $BVRI$ bands were plotted on a V vs $V - I$ CM diagram. All but seven of the optically detected stars are

foreground stars. Since seven sources is not statistically significant for the young cluster, we instead plot the J vs $J - H$ CM diagram in Fig. 6. In this plot the slanting arrow denotes the reddening vector associated with 15 mag of extinction. YSOs identified in the JHK CC diagram in Fig. 4 are shown as open circles; triangles mark the bright stars.

PMS evolutionary tracks (Palla & Stahler 1999) for ages 1, 3 and 5 Myrs are shown in Fig. 6 with dotted, short-dashed, and long-dashed lines, respectively. We have assumed a distance of 4.2 kpc (Molinari et al. 1996) and have reddened the isochrones with the average extinction of $A_V = 7.6$ mag estimated from the JHK CC diagram analysis in Sect. 3.1. Given the poor statistics for this distant cluster, it is not easy to derive the age by isochrone fitting. Even for regions with good statistics, it is quite difficult to constrain the age because most low mass stars spend the bulk of their PMS time on the Hayashi track, which is the *vertical* part of each isochrone. However, a small fraction of observed young stars will coincide with the brief evolutionary phase associated with the Henyey track, which is the *horizontal* transition between the Hayashi track and the Zero-Age-Main Sequence (ZAMS) (see e.g. Ascenso et al. 2007).

In Fig. 6 we note that there is a large population of low mass/low J magnitude candidate young stars (open circles) that lie to the *right* of the 1 Myr isochrone (dotted line). Some of these sources may be Class I protostars associated with the cluster. However, most will be Class II sources (T Tauri stars) with an age of about 1 Myr; many of these sources lie to the right of the 1 Myr isochrone because of extinction which, to these embedded sources, will be higher than the $A_V \sim 8$ mags used to deredden the PMS isochrones. However, there is also a population of candidate low mass young stars that lie to the *left* of the 1 Myr isochrone. These sources represent a more evolved group of young stars that are probably 3 Myr or older. Indeed, there are five probable cluster members that align horizontally and may therefore represent the Henyey part of the 3 Myr isochrone (short dash). Hence, we estimate that there is a low mass population of stars associated with IRAS 19343+2026 that is best represented by an age of 1 Myr or more. The mass range plotted in the figure is from $0.6 M_\odot$ to $3.0 M_\odot$ for the 3 Myr isochrone. The 5 Myr isochrone (long dash; mass range $0.6 - 2.5 M_\odot$) may well be within the age spread of the cluster. However, it extends beyond the limits of the observed data points.

One should also note that the J vs $J - H$ diagram contains only 333 sources that are common to the J and H bands. This is a considerable under-representation of the full sample, given that 875 sources are detected in the K band and that many of the fainter, redder

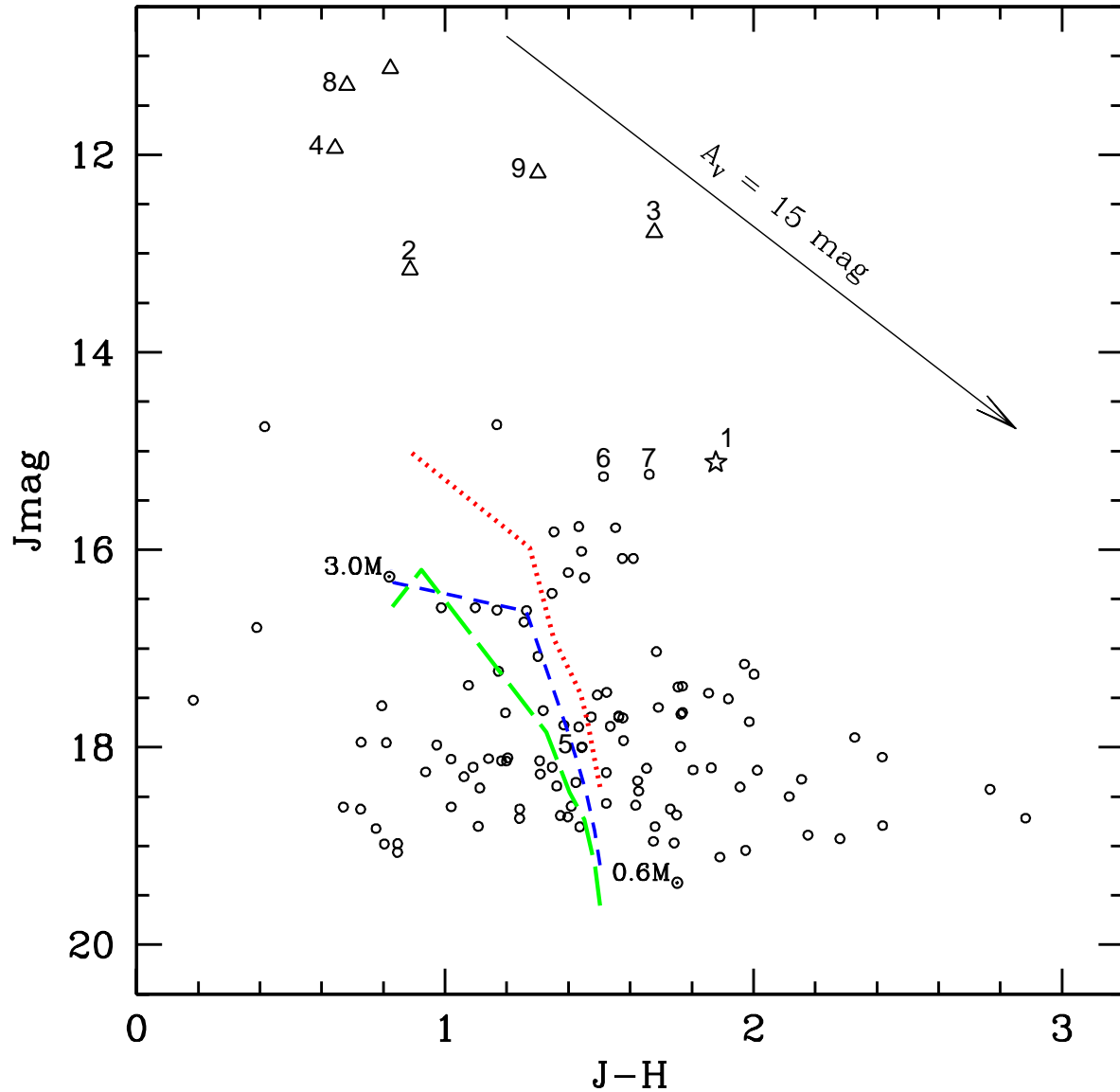


Figure 6. J vs $J - H$ CM diagram from the UFTI data. Open circles are probable cluster members as estimated from the $J - H/H - K$ CC diagram in Fig. 4. The triangles mark the brightest NIR sources in the region, while the numbers refer to the sources labelled in Fig. 1. The star symbol (star 1) marks the $2 \mu\text{m}$ source that coincides with the FIR peak. The PMS 1 Myr, 3 Myr (range = $0.6 M_{\odot} - 3.0 M_{\odot}$; marked) and 5 Myr (range = $0.6 M_{\odot} - 2.5 M_{\odot}$) isochrones (Palla & Stahler 1999) are drawn using dotted, short-dashed and long-dashed lines. The slanting solid line shows the reddening vector.

sources will be detected only at longer wavelengths. Nevertheless, the sample is statistically significant when comparing with evolutionary tracks and obtaining an age estimate for the low mass sources in this region.

3.2 The Initial Mass Function

As a next step to better understanding this region, we evaluate the mass function of the cluster. In the NIR, young stars are best detected in the K -band. Consequently, we use

the K -band Luminosity function (KLF) to evaluate this statistically important parameter. Ideally, we want to build the KLF using UFTI data which has a higher spatial resolution compared to the UKIDSS data. But the estimate of the mass function should be compared with the mass function of the control field, which is not possible using UFTI data, since we do not have control field images obtained with UFTI. The number of sources detected in the UFTI and UKIDSS images is very similar (to within 5%) for the same FOV. Therefore, we will evaluate the initial mass function (IMF) using the UKIDSS data which is uniformly calibrated for both the cluster and control regions.

By using the control region comparison, the differences arising due to contamination from the foreground and background members are accounted for. Although we identified probable cluster members (T Tauri and related sources) in Sec. 3.1, this identification was based on using only those stars that appear in the J , H and K bands. However, there are roughly twice as many stars detected in the K -band, whose cluster membership can not be easily verified. Therefore, we have used statistical criteria to estimate the number of probable member stars in the cluster region. To remove contamination of field stars from the cluster region sample, we have statistically subtracted the contribution of field stars from the CM diagram of the cluster region using the following procedure. For a randomly selected star in the K , $(H - K)$ CM diagram of the control region (see Fig. 5), the nearest star in the cluster's K , $(H - K)$ CM diagram within $K \pm 1.0$ and $(H - K) \pm 0.5$ of the field star was removed. The statistically cleaned K , $(H - K)$ CM diagram of the cluster region is shown in Fig. 5 (*right*) which clearly shows the presence of PMS stars in the cluster. With the help of this statistically cleaned CM diagram, we compute the IMF (e.g., Ojha et al. 2009). The K -band luminosities are corrected by the mean extinction determined by dereddening the stars on the CC diagram (see Sect. 3.1) which is $A_V \sim 8.0$ mag. The de-reddened magnitudes were then used to construct a reddening-corrected KLF. Stellar masses for the assumed 3 Myr old cluster members were obtained using the evolutionary models of Geneva (Lejeune & Schaerer 2001) and Palla & Stahler (1999). The MF of the statistically cleaned cluster region sources was obtained by counting the number of stars in various mass bins and is shown in Fig. 7. The vertical dashed and dot-dashed lines represent 90% and 100% completeness limits obtained for the UKIDSS GPS data, respectively.

The MF of the IRAS 19343+2026 region appears to rise monotonically up to $\sim 1.0 M_\odot$. The MF has a slope ($d\text{Log}(N)/\text{Log}(M)$) of -1.12 ± 0.16 for the probable cluster members sample over the mass range $1.0 < M/M_\odot < 6.3$. The classical value derived by Salpeter

(1955) is -1.35. Comparison of the MF of the IRAS 19343+2026 region with that of the Trapezium cluster (slope = -1.21 for $M/M_{\odot} > 0.6$) measured by Muench et al. (2002) reveals a resemblance, in the sense that both MFs rise monotonically beyond $M/M_{\odot} > 0.6$. The cluster region slope is shallower than the Salpeter value (-1.35). This indicates that the star formation process is not yet complete in the region. Star formation is ongoing, although previous episodes of star formation activity have resulted in a significantly low mass content. This situation represents active star formation over a period of 3 – 5 Myr as observed in other examples of massive star forming regions (Ascenso et al. 2007).

We have also estimated the mass of the cluster by integrating the observed mass function above the completeness limit ($\log M_{\text{lim}} \sim 0.1 M_{\odot}$ from Fig. 7). A mass of $\sim 307 M_{\odot}$ is obtained. For the masses below the completeness limit, we have extrapolated the theoretical IMF slopes from Kroupa (2001) down to the brown dwarf limit (see Fig. 7). The integration over the IMF yields a total cluster mass, $M_{\text{total}} \sim 585 M_{\odot}$. This is comparable to the masses of clusters such as those associated with the Trapezium and Mon R2 (Lada & Lada 2003).

3.3 Spectroscopy

Long-slit *HK* band spectra of two bright and five faint sources were obtained to investigate the nature of the stellar sources in the cluster. In Fig. 1, the straight lines mark the positioning of the slit which, for each exposure, covered multiple stars. The numbers by the side of the line identify the stars seen through the slit. In Fig. 8 the spectra of each of these stars are shown. The stars 1, 2 and 3 are the bright stars that are close to the FIR emission peak. Stars 4, 5, 6 and 7 are fainter (presumably low mass) stars that lie in the central regions of the cluster. Stars 3, 5, 6 and 7 occupy the T Tauri zone in our *JHK* CC diagram in Fig. 4, while star 1 lies in the HAeBe zone of this plot.

The two bright stars (1 & 3) that coincide with the FIR peak (see Fig. 1) display the HI Bracket series of lines indicating ionised emission. Note that star 2, which lies in between stars 1 and 3 on the slit, does not show the same recombination lines. The HI lines are thought to arise very close to the star, since the $120''$ long slit encompasses the dense nebula and we see no signature of extended nebular emission. As will be shown in the next section, the SED modelling of these bright objects classifies them as massive young stars. Star 1, the best massive protostellar candidate in the region, shows intense Pa α emission, in addition to the HI recombination lines. Both stars, 1 and 3, display a rising slope long-ward of 2

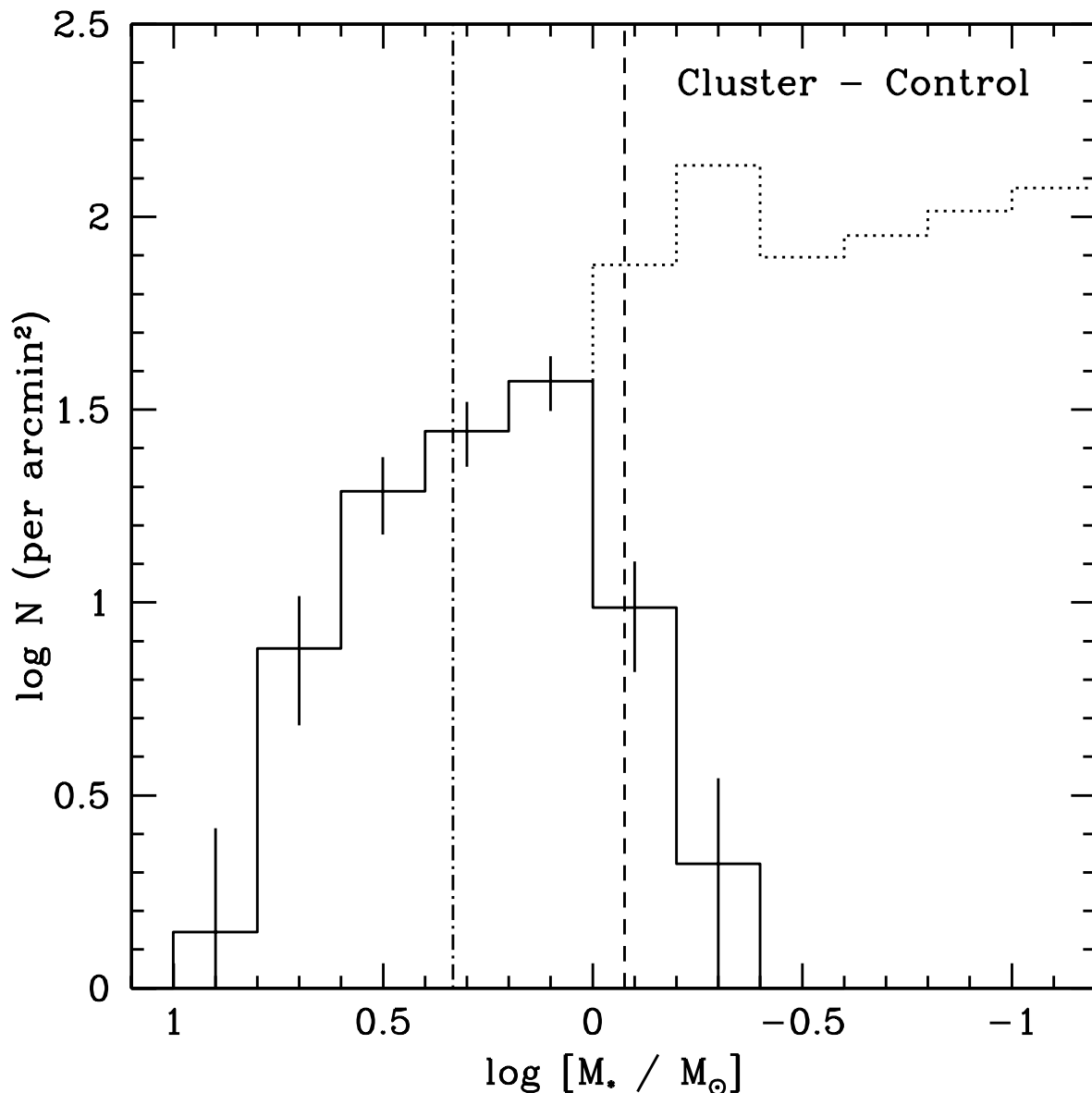


Figure 7. The mass function (with $\pm\sqrt{N}$ error bars) of the statistically cleaned IRAS 19343+2026 cluster region derived from the UKIDSS data. The plot is based on the evolutionary models of Lejeune & Schaerer (2001) and Palla & Stahler (1999), for an assumed age of 3 Myr. The vertical dashed and dot-dashed lines represent 90% and 100% completeness limits, respectively. The dotted line shows the theoretical IMF from Kroupa (2001), for the masses below the completeness limit ($\log M_{\text{lim}} \sim 0.1 M_{\odot}$).

μm . Together, these features indicate that stars 1 and 3 are early B type stars capable of producing an ionised sphere around themselves (Osterbrock 1989). Main-sequence B stars are characterised by HI absorption features which become weaker for more massive stars. However, for O type stars, helium absorption features appear and become prominent with increasing mass (Hanson et al. 2005). Neither HI nor He absorption features are visible in the bright stars 1 and 3, suggesting that the photospheres are likely obscured by the surrounding compact HII region and dense material.

In contrast, the remaining spectra of fainter stars (4, 5, 6 & 7) are featureless, and display a slope that is either flat or rising short-ward of $2 \mu\text{m}$. The absence of any emission features suggests a relatively evolved T Tauri star (Antoniucci et al. 2008), while the absence of any absorption features would suggest heavy veiling (Greene & Lada 1996, and references therein). Therefore, the fainter stars 4, 5, 6 & 7 are best matched by T Tauri type stars. The stars 6 & 7 are separated by a projected angle of $1.5''$; both show a common spectral feature at $2.4 \mu\text{m}$. This broad feature was not identified with any known spectral lines. The feature is likely to be a poorly removed telluric absorption feature (owing to poor sky beyond $2.3 \mu\text{m}$) and/or a local artifact in the slit. We note that there is no such spectral feature known in previous literature, even in the most embedded sources with lots of emission lines.

3.4 SED modelling of bright stars

The four bright stars that dominate the central region of the infrared nebula, namely stars 1, 3, 8 and 9 (see Fig. 1), are resolved in the *Spitzer* IRAC bands for which point source photometry is available. Note that these four stars are the brightest NIR sources associated with the IRAS 19343+2026 cluster (see Table 1). Only stars 1, 3 and 8 were detected in the MIPS $24 \mu\text{m}$ images. Stars 3, 8 and 9 are also detected in our optical *BVRI* images. Of these, star 8 is a multiple star with unreliable photometry since the PSF is larger than the separation of the multiple components. Therefore, the optical magnitudes of star 8 are used as upper limits in the modelling.

The SEDs of these four sources were modelled using the online SED fitting tool developed by Robitaille et al. (2007). The results of the SED modelling are summarised in Table 2. In Fig. 9, the observed data points (shown as black dots and filled triangles) and the fitted SED models are plotted. The solid black line shows the best fit model while the grey lines represent models that satisfy the criteria of $\chi^2 - \chi^2_{best} < 3$, where χ^2 is per data point. The weighted means and standard deviations in Table 2 are calculated using all of the parameters from the models that satisfy the above criteria. The weight is the inverse of the χ^2 value. The standard deviations quoted in Table 2 help the reader to visualize the spread in the range of values between multiple models that satisfy the above criteria. The dotted line represents the photospheric emission assumed in the model.

It is interesting to note that the FIR peak (star 1) is a young massive star of $\sim 7.6 M_{\odot}$ which is deeply embedded in an envelope. The remaining bright stars are 6 - $7 M_{\odot}$ objects

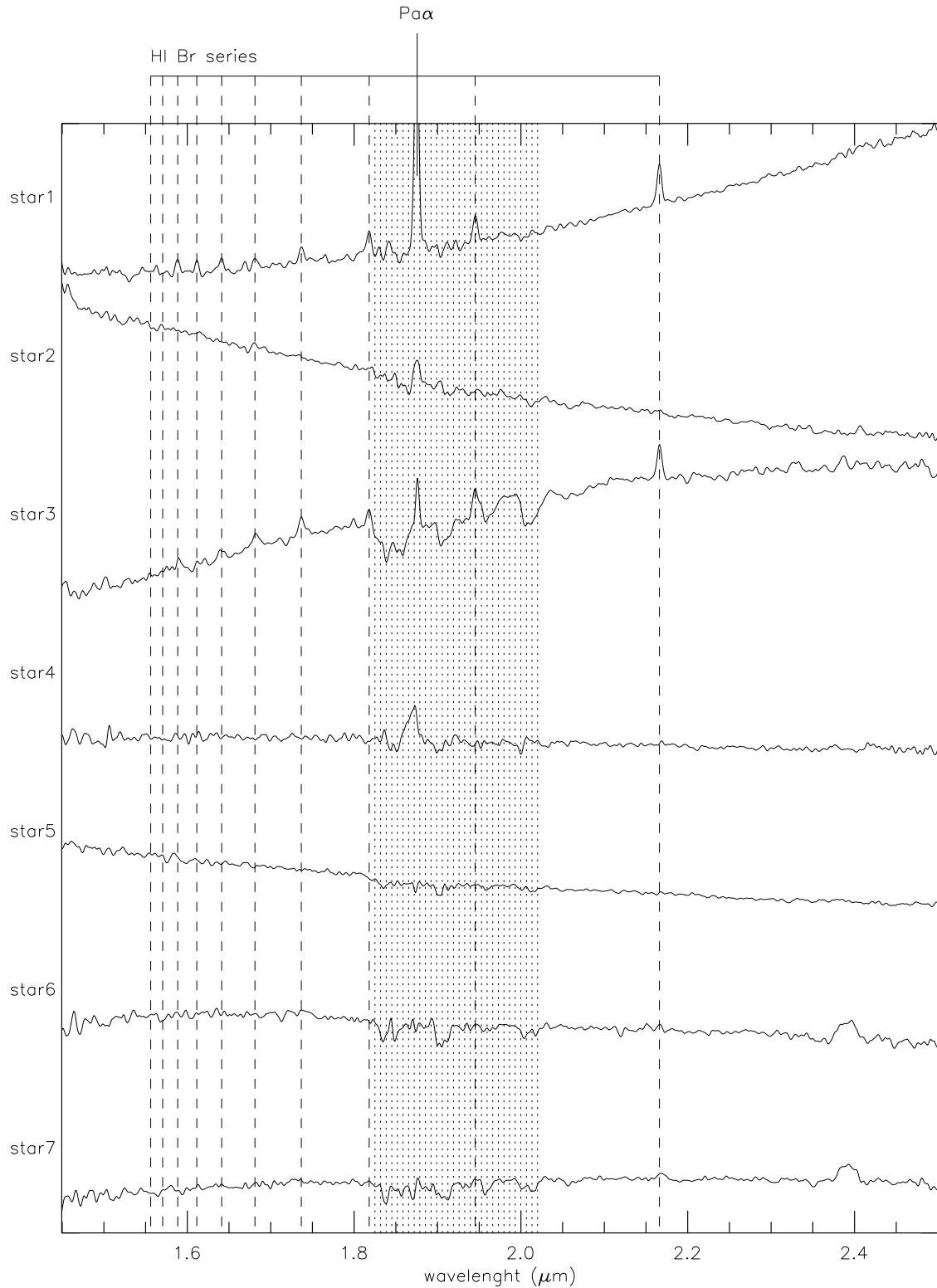


Figure 8. *HK* band spectra of the stars marked in Fig. 1. The shaded area represents the region of poor atmospheric transmission.

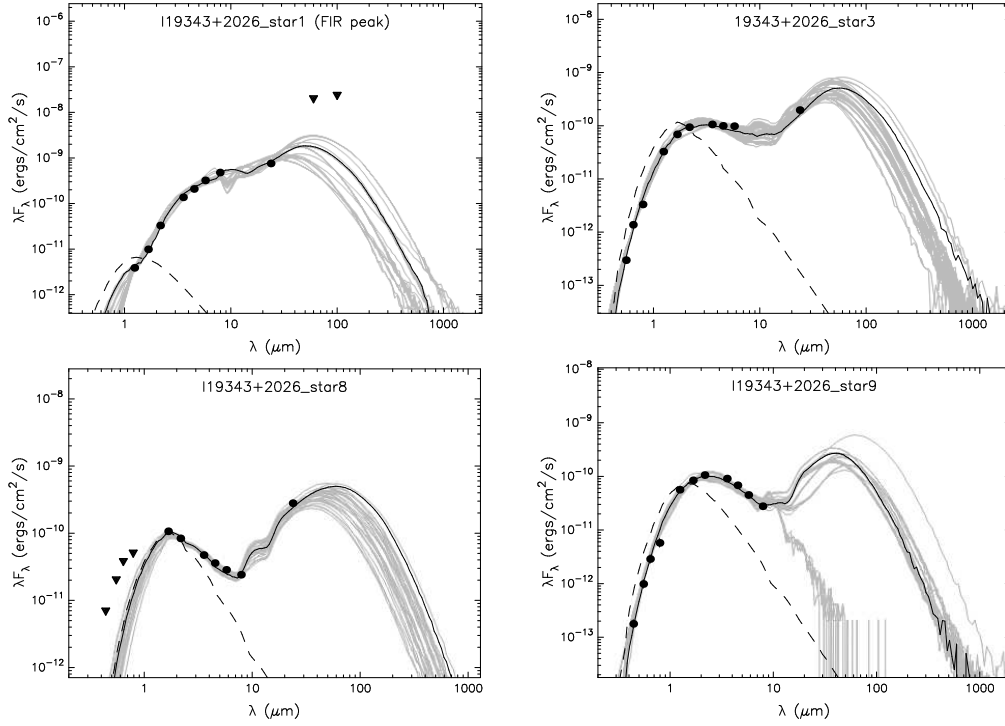


Figure 9. SEDs for the FIR peak, star 1, and three other candidate massive young stars. The black dots display photometric data points from 1 - 24 μm from 2MASS and *Spitzer*; filled triangles mark optical or IRAS 60 μm and 100 μm data. The solid grey curves denote the family of fitted models; the black curve represents the best fit (the dashed curve indicates the photosphere emission input to produce the best fit model). Note that these bright sources were saturated in the UFTI and UKIDSS data.

Table 1. Photometry used for SED modelling^{a,b}

| RA (2000) deg | DEC (2000) deg | <i>B</i> mag | <i>V</i> mag | <i>R</i> mag | <i>I</i> mag | <i>J</i> mag | <i>H</i> mag | <i>K</i> mag | 3.6 μm mag | 4.5 μm mag | 5.8 μm mag | 8.0 μm mag |
|------------------|-------------------|-----------------|-----------------|-----------------|-----------------|-----------------|-----------------|-----------------|--------------------------|--------------------------|--------------------------|--------------------------|
| 294.12900 | 20.55662 | - | - | - | - | 14.99 | 13.18 | 11.11 | 8.10 | 6.90 | 5.68 | 4.27 |
| 294.12899 | 20.55319 | - | 19.60 | 17.50 | 16.20 | 12.68 | 11.07 | 9.98 | 8.37 | 7.70 | 6.96 | - |
| 294.12634 | 20.55140 | 16.50 | 15.00 | 13.88 | 13.22 | 11.22 | 10.60 | 10.11 | 9.25 | 8.81 | 8.31 | 7.51 |
| 294.12489 | 20.55042 | 20.50 | 18.30 | 16.70 | 15.60 | 12.09 | 10.85 | 9.86 | 8.54 | 8.11 | 7.82 | 7.36 |

^a0.1 mag (10%) error is assumed on all magnitudes. See text for details.

^bThe UFTI *J, H, K* photometry of all the cluster members is available in the online table.

with nearly revealed photospheres surrounded by remnant dust envelopes (indicated by the second peak in the SED models). These results are consistent with the fact that star 1 is not optically visible, unlike stars 3, 8 and 9. The VLA NVSS survey shows centimeter free-free continuum emission coincident with the central region of this nebula. The cm continuum emission may represent the ionised gas in the central nebula associated with these four early B type stars.

Table 2. SED modelling results

| Source | χ^2 | Mass (M_\odot) | Log(Age) yr | $\log(M_{disk}) M_\odot$ | $\log(M_{env}) M_\odot$ | $\log(\dot{M}_{disk}) M_\odot \text{yr}^{-1}$ | $\log(\dot{M}_{env}) M_\odot \text{yr}^{-1}$ |
|--------|----------|--------------------|-------------|--------------------------|-------------------------|---|--|
| Star 1 | 10.0 | 7.6±0.6 | 5.2±0.6 | -1.5±0.7 | 1.2±0.7 | -6.8±1.1 | -4.3±0.6 |
| Star 3 | 28.8 | 6.3±0.8 | 5.4±0.3 | -2.0±1.0 | 0.8±0.7 | -7.2±1.2 | -5.1±0.9 |
| Star 8 | 14.6 | 6.1±0.6 | 4.6±0.3 | -1.8±0.7 | 0.9±0.6 | -7.0±0.9 | -3.8±0.4 |
| Star 9 | 16.7 | 7.4±1.8 | 5.5±0.4 | -2.5±2.2 | -1.0±2.5 | -7.2±2.3 | -4.8±0.5 |

4 CONCLUDING REMARKS

In the previous sections we characterised the stellar content associated with the massive protostellar object candidate, IRAS 19343+2026. The stellar content is composed of at least four young ($\sim 10^5$ yr) B type stars and a rich population of low mass stars at ~ 1 - 3 Myr. The FIR peak is modelled as a $7.6 M_\odot$ massive young star. The cluster is surrounded by a bright infrared nebula seen from 3–24 μm , indicative of dust and polycyclic aromatic hydrocarbons (PAH) emission. While the *Spitzer* IRAC and MIPS bands display the infrared nebula that becomes increasingly brighter from 3.6 μm to 24 μm , the NIR bands predominantly display the dense stellar population embedded in this nebula. The following facts can explain why the cluster population is better detected in deep *K* band images than in *Spitzer* images. The contribution of stellar photospheres rapidly falls off longward of 2 μm . Further, the background emission due to PAHs is strong in the bands longward of 4.5 μm . The above two facts, together with the relatively large PSF of the *Spitzer* data, reduces the sensitivity and contrast of the revealed low mass stars. However, the massive stars and the most embedded objects which appear bright at longer wavelengths are best revealed by the *Spitzer* images. This can explain why deeper NIR *K*-band data such as the one presented here can unveil the lower mass population better than the GLIMPSE survey.

The fainter and relatively older low mass population revealed by the NIR images are uniformly arranged over the infrared nebula (see Fig. 1), coinciding well with the warm dust distribution seen in 24 μm emission. As shown in Section 3.1, this population is best described to be 1 - 3 Myr old. In contrast, the four bright sources are found to be in the age range of $10^4 - 10^5$ yr (see Table 2). This suggests that low mass star formation occurred in the cluster prior to the formation of massive stars. Although this idea has been argued before, from observations of other regions (e.g. Kumar, Tafalla & Bachiller 2004), we arrive at the same conclusion based on a more rigorous analysis using a CM diagram, *HK*-band spectra, and SED modeling. If all embedded clusters are born with a universal IMF, then sampling the IMF at any given time, uniformly over all mass ranges, is naturally expected to result in

fewer massive stars and a greater number of low mass stars. Consequently, in the evolution of an embedded cluster (expected to follow an universal IMF), there exists an early phase when the total number of massive stars will be zero with a non-zero population of low mass stars. This simple statistical reasoning suggests that massive stars should appear after the low mass stars in a young cluster. Thus, it appears quite clear that the sequence for star formation is “low mass stars first and massive stars next”, at least for clusters forming B type stars. The situation for clusters forming O type stars requires further investigation.

5 ACKNOWLEDGMENTS

We thank the referee for useful comments that improved this manuscript. We are grateful to Stefan Schmeja for computing the nearest-neighbour densities from our photometric data that is used in Fig. 2. This research has received funding from the European Communities Seventh Framework Programme (FP7/2007-2013) under grant agreement SF-WF-MSF-230843. The United Kingdom Infrared Telescope is operated by the Joint Astronomy Centre on behalf of the U.K. Particle Physics and Astronomy Research Council. This work is based on data obtained as part of the UKIRT Infrared Deep Sky Survey. Kumar is supported by a Ciência 2007 contract, funded by FCT/MCTES (Portugal) and POPH/FSE (EC). This research made use of data products from the *Spitzer* Space Telescope GLIMPSE legacy survey. These data products are provided by the services of the Infrared Science Archive operated by the Infrared Processing and Analysis Center/California Institute of Technology, funded by the National Aeronautics and Space Administration and the National Science Foundation. We thank the staff of IAO, Hanle and CREST, Hosakote, that made these observations possible. The facilities at IAO and CREST are operated by the Indian Institute of Astrophysics, Bangalore. We would like to thank A.K. Pandey and M.R. Samal for helpful comments and discussion.

REFERENCES

- Antoniucci S., Nisini B., Giannini T., Lorenzetti L., 2008, *A&A*, 479, 503
- Ascenso, J., Alves, J., Vicente, S., Lago, M. T. V. T., 2007, *A&A*, 476, 199
- Baraffe I., Chabrier G., Allard F., Hauschildt P.H., 1998, *A&A*, 337, 403
- Bessell M.S., Brett J.M., 1988, *PASP*, 100, 1134
- Casali M., et al., 2007, *A&A*, 467, 777

- Cavanagh B., Hirst P., Jenness T., Economou F., Currie M. J., Todd S., Ryder S. D., 2003, in Payne H. E., Jedrzejewski R. I., Hook R. N., eds, ASP Conf. Ser. Vol. 295, *Astronomical Data Analysis Software and Systems XII*. Astron. Soc. Pac., San Francisco, p. 237
- Churchwell E., Babler B.L., Meade M.R. et al., 2009, *PASP*, 121, 213
- Grave J.M.C., Kumar M.S.N., 2009, *A&A*, 498, 147
- Greene T.P., Lada C.J., 1996, *AJ*, 112, 2184
- Hanson M.M., Kudritzki R.-P., Kenworthy M.A., Puls J., Tokunaga A.T., 2005, *ApJS*, 161, 154
- Hawarden T.G., Leggett S.K., Letawsky M.B., Ballantyne D.R., Casali M.M., 2001, *MNRAS*, 325, 563
- Kroupa P., 2001, *MNRAS*, 322, 231
- Kumar M.S.N., Tafalla M., Bachiller R., 2004, *A&A*, 426, 195
- Kumar M.S.N., Keto E., Clerkin E., 2006, *A&A*, 449, 1033
- Kumar M.S.N., Grave J.M.C., 2007, *A&A*, 472, 155
- Lada C.J., Adams F.C., 1992, *ApJ*, 393, 278
- Lada C.J., Lada E.A., 2003, *ARA&A*, 41, 57
- Landolt A.U., 1992, *AJ*, 104, 340
- Lawrence A., Warren S.J., Almaini O. et al., 2007, *MNRAS*, 379, 1599
- Lejeune T., Schaerer D., 2001, *A&A*, 366, 538
- Lucas P.W., Hoare M.G., Longmore A. et al., 2008, *MNRAS*, 391, 136
- McKee, C.F., Tan J.C., 2002, *Nature*, 416, 59
- McKee, C.F., Tan J.C., 2003, *ApJ*, 585, 850
- McNamara B.J., Sekiguchi K., 1986, *ApJ*, 310, 613
- Mercer, E.P., Clemens, D.P., Meade, M.R. et al., 2005, *ApJ*, 635, 560
- Meyer M.R., Calvet N., Hillenbrand L.A., 1997, *AJ*, 114, 288
- Molinari S., Brand J., Cesaroni R., Palla F., 1996, *A&A*, 308, 573
- Muench A.A., Lada E.A., Lada C.J., Alves J.F., 2002, *ApJ*, 573, 366
- Ojha D.K., Tamura M., Nakajima Y., Saito H., Pandey A.K., Ghosh S.K., Aoki K., 2009, *ApJ*, 693, 634
- Osterbrock D.E., 1989, *Astrophysics of Gaseous Nebulae and Active Galactic Nuclei*, University Science Books, Mill Valley, California
- Palla F., Stahler S., 1999, *ApJ*, 525, 772
- Ramsay Howat S.K., Todd, S., Leggett, S., Davis, C. J. et al. (11 authors), 2004, "The

Table A1. UFTI *JHK* photometric data of the stars in the region of IRAS 19343+2026. The complete table is available in electronic form only.

| RA (2000) deg | Dec. (2000) deg | <i>J</i> mag | <i>H</i> mag | <i>K</i> mag |
|------------------|--------------------|-----------------|-----------------|-----------------|
| 294.11121 | 20.55862 | 17.58 | 16.83 | 15.11 |
| 294.11145 | 20.56095 | 18.24 | 16.05 | 14.88 |
| 294.11163 | 20.53695 | 18.10 | 15.80 | 13.94 |
| 294.11176 | 20.55444 | 18.14 | 15.73 | 14.39 |
| 294.11270 | 20.56126 | 14.75 | 14.36 | 13.83 |
| 294.11313 | 20.54862 | 18.49 | 17.86 | 17.57 |
| 294.11334 | 20.54917 | 16.44 | 15.40 | 14.75 |
| 294.11356 | 20.54623 | 18.13 | 16.56 | 15.53 |
| 294.11362 | 20.53854 | 17.95 | 17.26 | 16.64 |
| 294.11411 | 20.53953 | 17.85 | 17.20 | 16.81 |

commissioning of and first results from the UIST imager spectrometer”, In Proc Spie 5492, UV and Gamma-Ray Space Telescope Systems, eds. Hasinger G, Turner M.J., p.1160.

Robitaille T.P., Whitney B.A., Indebetouw R., Wood K., Denzmore, P., 2006, ApJS, 157, 256

Robitaille T.P., Whitney B.A., Indebetouw R., Wood K., 2007, ApJS, 169, 328

Roche P.F., Lucas P.W., Mackay C.D. et al., 2002, Proc. SPIE 4841, Instrument Design and Performance for Optical/IR ground based telescopes, eds: M. Iye & A.F.Moorwood.

Salpeter, E.E., 1955, ApJ, 121, 161

Schmeja S., Kumar M.S.N., Ferreira B., 2008, MNRAS, 389, 1209

Simons D.A., Tokunaga A., 2002, PASP, 114, 169

Stetson P.B., 1987, PASP, 99, 191

Whittet D.C.B., van Breda I.G., 1980, MNRAS, 192, 467

Zinnecker H., Yorke H.W., 2007, ARA&A, 45, 481

Zinnecker H., Beuther H., 2008, in: ASP Conference Series, Vol. 387, Eds: Beuther, H., Linz, H., and Henning, H. San Francisco: Astronomical Society of the Pacific, p. 438

APPENDIX A: UFTI *JHK* PHOTOMETRIC DATA

Only a few lines of Table A1 are printed here. The complete form of the table is available online only.